Rayleigh–Bénard convection in a cubic cell under the effects of gas radiation up to Ra=1E9

Maxime Delort-Laval, Laurent Soucasse, Philippe Rivière, Anouar Soufiani

Highlights

Rayleigh-Bénard convection in a cubic cell under the effects of gas radiation up to Ra=10^9

M. Delort-Laval, L. Soucasse, Ph. Rivière, A. Soufiani

- Direct numerical simulations of coupled radiation and Rayleigh-Bénard convection in a cubic cell are performed in the range $10^3 \leqslant \mathrm{Ra} \leqslant 10^9$ for an air/H_2O/CO_2 mixture.
- Radiative transfer delays the onset of convection but promotes convection and increases the kinetic energy of the flow from $\mathrm{Ra} \geqslant 10^5$.
- Specific contributions of radiative transfer to the potential energy balance and the *thermal energy* balance are highlighted.
- Second order turbulence statistics are analysed in the range $10^7 \leqslant \mathrm{Ra} \leqslant 10^9$.

Rayleigh-Bénard convection in a cubic cell under the effects of gas radiation up to Ra=10^9

M. Delort-Laval[a], L. Soucasse[a], Ph. Rivière[a], A. Soufiani[a]

[a] *Laboratoire EM2C, CNRS, CentraleSupélec, Université Paris-Saclay, 8-10 rue Joliot Curie, 91192 Gif-sur-Yvette, France*

Abstract

This paper investigates radiative transfer effects on Rayleigh-Bénard convection in a cubic cell over a large range of Rayleigh numbers, from $\mathrm{Ra} = 10^3$ (below the onset of convection) to $\mathrm{Ra} = 10^9$ in the turbulent regime. Coupled direct numerical simulations are carried out for a radiating air/H_2O/CO_2 mixture at room temperature, using a Chebyshev spectral method for the flow and a ray-tracing method for the radiation field. For the highest Rayleigh numbers, a subgrid model is used to account for the radiation of the smallest, non-optically thin, turbulent scales. Symmetry and time-averaging (for unsteady solutions) are applied to compare coupled and uncoupled results, regardless of the multiple flow configurations that may be obtained. At low Rayleigh number, the potential energy decreases, and the onset of convection is delayed when radiation is taken into account. However, once convection settles, the potential energy increases with radiation, leading to a higher convective flux in the core and a higher kinetic energy. Specific contributions of radiative transfer to the potential energy balance and to the *thermal energy* balance are highlighted. It is also shown that the ratio of radiative and convective source terms in the energy balance roughly scales as $\mathrm{Ra}^{-1/2}$ and that radiative transfer effects weaken at high Rayleigh numbers. Finally, radiative transfer effects on turbulence budgets of mechanical and thermal fluctuations are analysed in the range $10^7 \leq \mathrm{Ra} \leq 10^9$. The magnitude of each term of these budgets is stronger when radiation is taken into account. However, radiative dissipation has little influence on the temperature fluctuation budget.

Email address: laurent.soucasse@centralesupelec.fr (L. Soucasse)

Preprint submitted to International Journal of Heat and Mass TransferDecember 14, 2021

Keywords: turbulent convection, radiative transfer, cubic Rayleigh-Bénard cell

1. Introduction

Rayleigh-Bénard (RB) convection, in which a fluid layer is heated from below and cooled from above, remains a challenging problem for both fundamental studies and for natural or engineering applications. These applications include atmospheric physics, convection in the Earth mantle, thermal management of buildings, and many industrial processes. A layer of transparent fluid heated from below is known to become unstable when the Rayleigh number reaches a critical value of about Ra_{cr} =1708 for an infinite geometry in the directions perpendicular to gravity, and for rigid walls [1]. When the fluid is confined in a closed cavity, the critical Rayleigh number increases due to friction on the lateral walls. Fluid confinement also leads to a great variety of possible flow structures and corresponding heat transfer rates just above the transition, due to the symmetries of the system. Several studies have revealed a variety of steady and unsteady flows at moderate Rayleigh numbers for a cubic cavity heated from below. Depending on the boundary conditions on the lateral walls, up to seven or nine (for insulated lateral walls [2, 3, 4]) or even more (for conducting lateral walls [5]) structures have been observed and analyzed using numerical simulations or continuation technique identification. The existence of multiple solutions at $\mathrm{Ra} = 10^5$ has also been observed experimentally depending on the initial conditions [6]. Different sets of the Nusselt number have indeed been identified for the same Rayleigh number. Also, benchmark numerical simulations in the range $10^5 - 10^8$ of the Rayleigh number have shown an important disparity between the results from several numerical codes [7].

Subsequently, several studies have shown that, for confined enclosures and intermediate Ra numbers, typically in the range $10^6 - 10^9$, the weakly turbulent RB flows are characterized by a Large-Scale Circulation (LSC) with low-frequency intermittent phenomena such as reversals and reorientations. Azimuthal rotation of the LSC and sudden reversals in cylindrical enclosures have been observed in experimental studies [8, 9] and by numerical simulations [10, 11]. Recently, large-scale flow reversals in circular enclosures have been demonstrated both experimentally [12] and numerically [13]. In cubic enclosures, LSC is generally organized in the diagonal vertical planes and reorientations from one plane to another have been observed [14, 15].

Several models have been developed to predict LSC low-frequency dynamics, either based on stochastic phenomenological approaches [16, 17, 18, 19, 20] or modal decomposition [21, 22, 23, 24, 25]. The development of such predictive models is a very attractive topic since Direct Numerical Simulations (DNS) must be run for very long integration times to capture these low-frequency phenomena.

The brief and non-exhaustive picture of the state of the art described above is related to RB convection in non-radiating fluids (transparent or opaque). However, it is well known that the small amounts of water vapour and carbon dioxide in ambient air are responsible of significant radiative transfer that could affect the mean and fluctuating temperature fields and the resulting thermal convection. This radiative transfer is at the origin of the greenhouse effect in Earth atmosphere. The effects of radiation on RB convection, with application to atmospheric physics, have been investigated in the pioneering studies [26, 27, 28]. Using linear stability analyses, radiative transfer was shown to delay the onset of instability due to two mechanisms, namely, the homogenization of the temperature field in the core of the fluid layer (effect on the base state) and the damping of temperature disturbances [29]. Numerical simulations [30, 31] and experimental studies [28] have also confirmed this behavior. However, the above mentioned studies were limited to the first transition to the convection regime or addressed the flow structure and heat transfer just above this transition.

For higher Rayleigh numbers, although several studies have addressed the effects of radiation on natural convection in differentially heated cavities [32, 33, 34, 35], there are very few studies related to radiation effects on RB convection in chaotic and turbulent regime. First attempts have been performed in Refs. [36, 37] for Rayleigh numbers of about $10^6 - 10^7$. However, no full coupling was considered in Ref. [36] and, in Ref. [37], devoted to mixed convection, the gray gas assumption was used for a non-confined thin layer of radiating fluid. A preliminary investigation [38] of radiation effects on RB convection in a cubic cell was limited to $\mathrm{Ra} = 10^7$ and, due to limitations in computational resources, the integration time was not sufficient to capture LSC reorientations. More recently, low order models based on Proper Orthogonal Decomposition (POD) have been developed to analyse these LSC reorientations with and without radiation [39, 40] in the range $10^6 \leqslant \mathrm{Ra} \leqslant 10^8$. Similar first eigenmodes were found with and without radiation but with higher energies (eigenvalues) when radiation was taken into account. It was found also that the frequency of reorientation events tends

to increase with radiative transfer. However, the effects of radiation on heat transfer and flow dynamics were not fully analyzed in these studies.

The aim of this paper is to analyse molecular radiation effects on heat transfer and flow dynamics in a large range of the Rayleigh number, from 10^3 to 10^9, in a cubic cavity heated from below and cooled from the top at constant temperatures, with insulated lateral walls. Mixture of air with small amounts of H_2O and CO_2 as radiating gases, typical of ambient humid air conditions, is considered. Given the variety of flow patterns (and associated reorientations in unsteady regime) that may be observed in the large range of Rayleigh numbers studied, we will focus the analysis on symmetry-averaged and time-averaged (for unsteady solutions) quantities. The governing equations and the employed numerical methods for DNS are described in Sec. 2. The symmetries of the considered problem are also discussed in this section. The effects of radiation on mean flow fields and on mean conductive, convective and radiative fluxes are discussed in Sec. 3. Then we analyse the budgets of kinetic energy, potential energy, and *thermal energy* (square of the temperature differences) in Sec. 4. Finally, in Sec. 5, second order statistics are processed in the range $10^7 \leqslant \mathrm{Ra} \leqslant 10^9$ to analyse the budgets of turbulent kinetic energy and of the variance of temperature fluctuations.

2. Direct numerical simulations

2.1. Problem set-up and governing equations

The studied configuration is displayed in Fig. 1. We consider a cubic cavity of size L, heated from below and cooled from above. Top and bottom walls are isothermal at temperature T_{cold} and T_{hot}, and are black (emissivity $\varepsilon = 1$). The four side walls are adiabatic and perfectly diffuse reflecting (emissivity $\varepsilon = 0$). The cavity is filled with a radiating air/H_2O/CO_2 mixture at a mean temperature T_0.

In the case of a non radiating fluid the problem would be fully controlled by two parameters: the Prandtl number $\mathrm{Pr} = \nu_f/a$ and the Rayleigh number

$$\mathrm{Ra} = \frac{g\beta\Delta T L^3}{\nu_f a}, \tag{1}$$

where g is the gravitational acceleration, $\beta = 1/T_0$ is the thermal expansion coefficient, $\Delta T = T_{\mathrm{hot}} - T_{\mathrm{cold}}$ is the temperature difference, ν_f is the kinematic viscosity and a is the thermal diffusivity. In the presence of gas radiation,

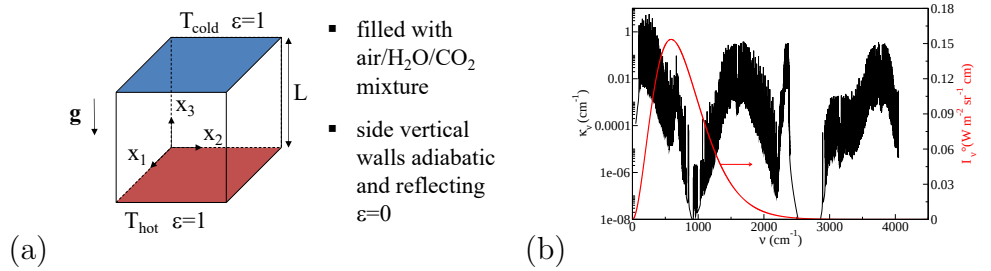

Figure 1: (a) Cubic Rayleigh-Bénard cavity filled with a radiating air/H_2O/CO_2 mixture. Top and bottom walls are isothermal and black while side vertical walls are adiabatic and perfectly diffuse reflecting. (b) Absorption coefficient spectrum of the considered air/H_2O/CO_2 mixture ($T_0 = 300$ K, $X_{H_2O} = 0.02, X_{CO_2} = 0.001$, atmospheric pressure) and Planck function $I^\circ_\nu(T_0)$.

it is not possible to define a limited set of dimensionless parameters due to the complex structure of molecular absorption spectra. In order to make our study relevant for building applications, we consider an air/H_2O/CO_2 mixture at a mean temperature of $T_0 = 300$ K, at atmospheric pressure, of molar composition $X_{H_2O} = 0.02$ and $X_{CO_2} = 0.001$. The cavity size is set to $L = 1$ m and we vary the Rayleigh number by changing the temperature difference ΔT, other parameters being fixed. Thermophysical properties are assumed to be uniform (low temperature differences), not affected by the small amount of water vapour and carbon dioxide, and constant at all Rayleigh numbers (thermal conductivity $\lambda = 0.0263$ W m^{-1} K^{-1}, thermal diffusivity $a = 2.25 \times 10^{-5}$ m^2 s^{-1}, Prandtl number Pr $= 0.707$).

Mass, momentum and energy balance write under Boussinesq approximation

$$\frac{\partial u_i}{\partial x_i} = 0, \tag{2}$$

$$\frac{\partial u_i}{\partial t} + u_j \frac{\partial u_i}{\partial x_j} = -\frac{\partial p}{\partial x_i} + \mathrm{Pr}\theta\delta_{i3} + \frac{\mathrm{Pr}}{\sqrt{\mathrm{Ra}}} \frac{\partial^2 u_i}{\partial x_j \partial x_j}, \tag{3}$$

$$\frac{\partial \theta}{\partial t} + u_i \frac{\partial \theta}{\partial x_i} = \frac{1}{\sqrt{\mathrm{Ra}}} \left(\frac{\partial^2 \theta}{\partial x_i \partial x_i} + \mathcal{P}_{\mathrm{rad}} \right), \tag{4}$$

where x_i is the i^{th} dimensionless Cartesian coordinate, u_i is the i^{th} dimensionless velocity vector component, p is the dimensionless motion pressure, $\theta = (T - T_0)/\Delta T$ is the dimensionless temperature and $\mathcal{P}_{\mathrm{rad}}$ is the dimensionless radiative power. Eqs. (2)-(4) are made dimensionless using the reference

time $L^2/(a\sqrt{\mathrm{Ra}})$ and the reference length L. A non-slip boundary condition is imposed on the velocity at the six walls and the thermal boundary conditions write

$$\left.\begin{array}{lll} \theta = 0.5 & \text{on} & x_3 = 0, \\ \theta = -0.5 & \text{on} & x_3 = 1, \\ \boldsymbol{\nabla}\theta\cdot\boldsymbol{n} = 0 & \text{on} & x_1 = 0,\ x_1 = 1,\ x_2 = 0,\ x_2 = 1. \end{array}\right\} \tag{5}$$

Note that there is no radiative flux on the reflecting adiabatic sidewalls. The Boussinesq approximation is fully justified in the present study since, at the highest considered value of the Rayleigh number $\mathrm{Ra} = 10^9$ and with the above numerical values, the relative temperature difference is $\Delta T/T_0 = 0.036$. This would imply insignificant non-Boussinesq effects according to Ref. [41] for instance.

The dimensionless radiative power is defined by

$$\mathcal{P}_{\mathrm{rad}}(\boldsymbol{x}) = \frac{L^2}{\lambda \Delta T} \int_\nu \kappa_\nu \left(\int_{4\pi} I_\nu(\boldsymbol{x}, \boldsymbol{\Omega})\, d\boldsymbol{\Omega} - 4\pi I^\circ_\nu(T(\boldsymbol{x})) \right) d\nu, \tag{6}$$

where $I_\nu(\boldsymbol{x}, \boldsymbol{\Omega})$ is the actual radiative intensity at wavenumber ν, position $\boldsymbol{x}$, and direction $\boldsymbol{\Omega}$ and $I^\circ_\nu(T(\boldsymbol{x}))$ is the Planck equilibrium intensity (blackbody intensity) at temperature T. The absorption coefficient κ_ν is assumed to be uniform in accordance with the Boussinesq approximation. The high resolution spectrum of the absorption coefficient of the considered mixture is shown in Fig. 1. It contains thousands of spectral lines which makes expensive the computation of the integral over the wavenumbers in Eq. (6). Therefore, we use the Absorption Distribution Function (ADF) model [42] which consists in substituting the integration over the wavenumber with an integration over the values of the absorption coefficient, for which a coarse logarithmic discretisation is sufficient. In the present study, the values of the absorption coefficient of Fig. 1 have been logarithmically discretised in 16 classes and the accuracy of the model has been shown to be better than 1 % [43]. Model parameters and computational details for the considered mixture are given in Refs. [44, 32].

Using the ADF model, the dimensionless radiative power writes

$$\mathcal{P}_{\mathrm{rad}}(\boldsymbol{x}) = \frac{L^2}{\lambda \Delta T} \sum_k \kappa_k \left(\int_{4\pi} I_k(\boldsymbol{x}, \boldsymbol{\Omega})\, d\boldsymbol{\Omega} - 4 w_k \sigma T^4(\boldsymbol{x}) \right), \tag{7}$$

where κ_k and w_k are respectively the absorption coefficient and the weight associated with the k^{th} ADF class and σ is the Stefan-Boltzmann constant. The radiative intensity $I_k(\boldsymbol{x}, \boldsymbol{\Omega})$ is obtained by solving the radiative transfer equation for a non scattering medium, for each class k

$$\boldsymbol{\Omega} \cdot \boldsymbol{\nabla} I_k(\boldsymbol{x}, \boldsymbol{\Omega}) = \kappa_k \left(\frac{w_k \sigma T^4(\boldsymbol{x})}{\pi} - I_k(\boldsymbol{x}, \boldsymbol{\Omega}) \right). \tag{8}$$

The associated boundary condition at wall positions $\boldsymbol{x}^w$ for propagation directions $\boldsymbol{\Omega}$ such that $\boldsymbol{\Omega} \cdot \boldsymbol{n} > 0$, $\boldsymbol{n}$ being the wall normal directed towards the interior of the domain, writes

$$I_k(\boldsymbol{x}^w, \boldsymbol{\Omega}) = \frac{\varepsilon w_k \sigma T^4(\boldsymbol{x}^w)}{\pi} + \frac{1-\varepsilon}{\pi} \int_{\boldsymbol{\Omega}' \cdot \boldsymbol{n} < 0} I_k(\boldsymbol{x}^w, \boldsymbol{\Omega}') |\boldsymbol{\Omega}' \cdot \boldsymbol{n}| \, d\boldsymbol{\Omega}'. \tag{9}$$

2.2. Numerical methods

Direct Numerical Simulations (DNS) have been performed, considering the air/H_2O/CO_2 mixture as radiating (radiation case) or transparent (no-radiation case, $X_{H_2O} = 0$, $X_{CO_2} = 0$ and thus $\mathcal{P}_{\text{rad}} = 0$) for 12 Rayleigh number values in the range $10^3 \leq \text{Ra} \leq 10^9$. The coupled algorithm for solving flow equations (2)-(4) and radiative transfer equation (8) has been extensively used and described in previous works, for both differentially heated cavities [32, 33] and Rayleigh-Bénard cavities [39, 40]. We will briefly recall here the main features of this algorithm. Simulation parameters are given in Tab. 1.

Flow equations are solved using a collocation spectral method [45, 46] based on a Chebyshev polynomial expansion for the three directions of space. Time integration is performed through a second-order semi-implicit scheme. The pressure-flow coupling is ensured by a projection method that forces the velocity divergence free condition. Domain decomposition is applied along the vertical direction to perform parallel computations. The convection mesh is built from Chebyshev collocation points and is given in Tab. 1 for each Rayleigh number. We have checked that the number of points in the boundary layers is sufficient regarding the criterion proposed in Ref. [47]. Although this criterion was established for non-radiating fluids, calculation results show a posteriori that radiation does not affect so much the thickness of boundary layers. We therefore adopt the same meshing for flow filed calculations with and without radiation. The radiative transfer equation is solved using a ray-tracing algorithm [43, 32], made parallel by distributing

the rays among the different processors. The 4π steradian angular domain is uniformly discretized using between 900 rays to 3600 rays from volume cell centers, depending on the spatial mesh size. Up to $\mathrm{Ra} = 10^7$, the radiation mesh is built from the convection mesh, coarsened by a factor of two in each direction of space. For $\mathrm{Ra} \geq 3 \times 10^7$, the radiation mesh is built from the convection mesh, coarsened by a factor of four to eight in each direction of space and we use a subgrid model [48, 33] to account for the radiation of small spatial scales. This subgrid model has been validated in various configurations and its accuracy is about a few percent on radiative power and wall fluxes.

Finally, an explicit coupling is carried out between flow and radiation calculations and the radiation source term is updated every 10 convection time steps δt (every 5 convection time steps at $\mathrm{Ra} = 10^9$). Indeed, the flow time step is imposed by numerical stability constraints and does not correspond to significant variations of the temperature field. Note that the computed radiative source term is based on instantaneous temperature fields and will be discussed itself in terms of mean and fluctuating fields (see Sec. 5). For unsteady solutions, time integration is carried out over a period Δt once the asymptotic regime (statistically steady) is reached. It should be mentioned here that radiation calculations are much more computationally expensive than convection calculations (the CPU time is about 30 times greater in the radiation case).

2.3. Validation of the numerical tools

Validations of the pseudo-spectral solver were provided first in Ref. [43], where steady solutions of the natural convection problem for differentially heated cavities at different Rayleigh numbers varying from $\mathrm{Ra} = 10^5$ to 10^7, without radiation, were calculated and successfully compared with the 3D benchmark solutions of Ref. [49]. For weakly turbulent natural convection without radiation, the predictions from the present solver were compared with the results provided by Refs. [50, 51, 52] in the case of a parallelepipedic differentially heated cavity of aspect ratio $L_z/L_x = 4$, $L_y/L_x = 1$, filled with air ($\mathrm{Pr} = 0.71$), at a Rayleigh number based on the height of the cavity $\mathrm{Ra} = 2 \times 10^9$. Excellent agreement was found for both mean fields and second order statistics [32]. Moreover, the grid convergence was discussed in Ref. [33] for differentially heated cubic cavities at Rayleigh numbers up to $\mathrm{Ra} = 3 \times 10^9$.

For Rayleigh-Bénard convection in cubic cavities and without radiation, we compare in Tab. 2 the Nusselt number (dimensionless conductive flux av-

Ra	Convection mesh	Radiation mesh	$\delta t \times 10^3$	Δt
10^3	41x41x(4x11)	20x20x20	10	N/A
3×10^3	41x41x(4x11)	20x20x20	10	N/A
10^4	41x41x(4x11)	20x20x20	10	N/A
3×10^4	41x41x(4x11)	20x20x20	10	N/A
10^5	65x65x(4x17)	32x32x32	10	N/A
3×10^5	65x65x(4x17)	32x32x32	10	10,000 | N/A[(a)]
10^6	81x81x(4x21)	40x40x40	5	10,000
3×10^6	81x81x(4x21)	40x40x40	2.5	10,000
10^7	81x81x(4x21)	40x40x40	2.5	10,000
3×10^7	121x121x(6x21)	30x30x30[(b)]	2 | 1.5[(a)]	5,000
10^8	161x161x(8x21)	40x40x40[(b)]	1	5,000
10^9	321x321x(16x41)	40x40x40[(b)]	0.5 | 0.25[(a)]	100

Table 1: Simulation parameters: Convection mesh, radiation mesh, convection time step δt and integration time interval Δt for unsteady solutions. For the convection mesh, numbers in parenthesis indicate the number of spatial domains times the number of collocation points in the vertical in each domain. [(a)] No-radiation case | radiation case. [(b)]Radiation subgrid model is used.

Ra	10^6	10^7	10^8
Kaczorowski *et al.* (2013) [53], DNS, Pr = 0.7	8.32	16.30	31.30
Giannakis *et al.* (2018) [23], DNS, Pr = 0.7	-	16.57	-
Foroozani *et al.* (2017) [15], LES, Pr = 0.7	8.10	-	31.60
Xu et al. (2019) [54], LB, Pr = 0.7	8.33	16.22	-
Our results, DNS, Pr = 0.707	8.30	16.24	31.06

Table 2: Comparison of the averaged wall conductive Nusselt number with literature.

eraged over the hot and cold walls) computed in the present study with the few values found in the literature. A good agreement is obtained with differences smaller than 1% with the DNS results of Kaczorowski *et al.* (2013) [53], 2% with the DNS results of Giannakis *et al.* (2018) [23], 2.5% with the Large-Eddy Simulation (LES) results of Foroozani *et al.* (2017) [15], and 0.4% with the Lattice-Boltzmann (LB) results of Xu *et al.* (2019) [54]. Note that the 1% difference for the values of the Prandtl number used by the different authors are not expected to affect the Nusselt numbers by more than 1% according to the classical correlations that may be found in the literature [55].

In addition to the Nusselt number, we compare in Tab. 3 the flow strengths obtained in the present study with the LB computations of Xu *et al.* (2019) [54].

	$\mathrm{Re}^{\mathrm{rms}}$			$\mathrm{Re}^{\mathrm{rms}}_{u_3}$		
Ra	10^6	3×10^6	10^7	10^6	3×10^6	10^7
Xu *et al.* (2019) [54], LB, Pr=0.7	208.80	357.11	654.86	145.58	249.96	454.92
Our results, DNS, Pr=0.707	208.05	357.44	650.73	144.45	249.43	451.79

Table 3: Comparison of the flow strength with results of Xu et al. (2019) [54].

The flow strengths are characterized by the two Reynolds numbers $\mathrm{Re}^{\mathrm{rms}} = \sqrt{\langle\overline{u_i u_i}\rangle_v \mathrm{Ra}}/\mathrm{Pr}$ and $\mathrm{Re}^{\mathrm{rms}}_{u_3} = \sqrt{\langle\overline{u_3 u_3}\rangle_v \mathrm{Ra}}/\mathrm{Pr}$, based either on the total velocity magnitude or the vertical velocity magnitude ($\bar{\cdot}$ denotes the statistical average and $\langle\cdot\rangle_v$ the average over the entire volume of the cavity). The comparisons given in Tab. 3 show an excellent agreement with less than 1% differences in all cases.

As for radiative transfer computations, the ray-tracing algorithm was successfully compared to Monte Carlo results in the case of prescribed analytical temperature fields in a cubical enclosure [43]. The accuracy of the refined angular discretization and of the ADF model were studied in Ref. [44] and Ref. [43], respectively, and the radiation subgrid-scale model was validated, considering a snapshot of turbulent natural convection in a differentially heated cavity at $\mathrm{Ra} = 3\times10^9$ [48].

2.4. Symmetries

Without radiative source term, Eqs. (2)-(4) satisfy four independent reflection symmetries S_{x_1}, S_{x_2}, S_{x_3} and S_d with respect to the planes $x_1 = 0.5$, $x_2 = 0.5$, $x_3 = 0.5$ and $x_1 = x_2$ [5]. These symmetries act on the velocity and temperature fields as follows

$$S_{x_1}: \left.\begin{array}{l}(x_1,x_2,x_3)\to(1-x_1,x_2,x_3)\\(u_1,u_2,u_3,\theta)\to(-u_1,u_2,u_3,\theta)\end{array}\right\} \tag{10}$$

$$S_{x_2}: \left.\begin{array}{l}(x_1,x_2,x_3)\to(x_1,1-x_2,x_3)\\(u_1,u_2,u_3,\theta)\to(u_1,-u_2,u_3,\theta)\end{array}\right\} \tag{11}$$

$$S_{x_3}: \left.\begin{array}{l}(x_1,x_2,x_3)\to(x_1,x_2,1-x_3)\\(u_1,u_2,u_3,\theta)\to(u_1,u_2,-u_3,-\theta)\end{array}\right\} \tag{12}$$

$$S_{d}: \left.\begin{array}{l}(x_1,x_2,x_3)\to(x_2,x_1,x_3)\\(u_1,u_2,u_3,\theta)\to(u_2,u_1,u_3,\theta)\end{array}\right\} \tag{13}$$

These four elementary symmetries generate a symmetry group of sixteen elements. Radiation emission being proportional to T^4, radiative transfer should

break the S_{x_3} symmetry as the mean temperature gradient is directed along the x_3 axis. However, owing to the weak temperature gradients ($\Delta T \simeq 10$ K for the highest Rayleigh number), non-linear effects are negligible (namely $1 - \frac{4T_0^3 \Delta T}{T_{\rm hot}^4 - T_{\rm cold}^4} \simeq 3 \times 10^{-4}$ for the highest Rayleigh number) so that we can consider that the S_{x_3} symmetry is still satisfied in the radiation case. Symmetries (10)-(13) act on the radiative power field in the same way as they act on the temperature field.

These many symmetries are responsible for multiple flow patterns in the studied Rayleigh range. In the no-radiation case, symmetry breaking solutions are observed from the onset of convection at a critical Rayleigh number $\mathrm{Ra}_c \simeq 3400$ [56, 3]: one observes a single roll flow pattern around either the x_1 axis or the x_2 axis (which breaks either the S_{x_2} or S_{x_1} symmetry, and also the S_d symmetry). When the Rayleigh number increases up to the onset of unsteadiness, multiple stable or unstable flow patterns have been identified, as highlighted in Sec. 1. A detailed description of these flow patterns and associated bifurcation diagram, from the onset of convection and up to $\mathrm{Ra} = 1.5 \times 10^5$, for $\mathrm{Pr} = 0.71$ in a cubic cell, is provided in Ref. [3] for the no-radiation case. At higher Rayleigh numbers $\mathrm{Ra} \geq 10^6$ in unsteady regime, large-scale single roll flow patterns are observed, aligned along the diagonal planes $x_1 = x_2$ or $x_1 = 1 - x_2$ and breaking both S_{x_1} and S_{x_2} symmetries. However, all symmetries could be recovered for sufficiently long integration time, because of low-frequency reorientations of this large-scale roll in the horizontal plane, that are rotations of $\pi/2$ around the vertical axis [19, 15]. Reorientations of the large-scale roll in the horizontal plane have also been reported in the case of a radiating gas in the range $10^6 \leq \mathrm{Ra} \leq 10^8$ [40], radiation causing an increase of the reorientation frequency.

Given the variety of flow patterns that may be observed, it might seem difficult to compare the results of the radiation case and the no-radiation case. Therefore, we apply the symmetries to any flow variable ϕ after the simulation and we define the statistical average as follows

$$\overline{\phi} = \frac{1}{\Delta t} \int_{\Delta t} \frac{1}{16} \sum_{n=1}^{16} S_n(\phi)\, dt, \tag{14}$$

$S_n(\phi)$ being the action of the $n^{\rm th}$ symmetry (among 16 elements) of the symmetry group on the variable ϕ. The time average in Eq. (14) is only applied in the asymptotic regime of unsteady solutions.

3. Flow fields and heat transfer

In this section, we analyse the vertical distribution of key quantities averaged over horizontal planes. Statistical average (time average and symmetry average) as defined in Eq. (14) is applied to each solution.

3.1. Low Rayleigh numbers: onset of convection

Figure 2 shows the temperature, the kinetic energy and the radiative power (defined as the difference between the absorbed and emitted powers) obtained at the different Rayleigh numbers, in the radiation case and in the no-radiation case. At the lowest Rayleigh number (10^3), there is no kinetic energy for both the radiation and no-radiation case, which means that the convection has not started. The configuration is purely conductive in the no-radiation case, which means that the temperature profile is linear. However, the presence of radiative energy transfer in the radiation case diminishes the temperature gradient in the center of the cavity: gas-gas radiative exchanges tend to homogenise the temperature field in the cavity. When the Rayleigh number increases (between $\mathrm{Ra} = 3 \times 10^3$ and $\mathrm{Ra} = 10^4$), the convection settles in the no-radiation case, thus mixing the fluid and flattening the temperature profile. In the radiation case, though, the convection does not settle: the radiation has a delaying effect on the onset of the flow in the cavity. The gas is rather emitting near the hot wall and absorbing near the cold wall, and these radiative exchanges make the temperature field more stable.

But when the convection starts in the radiation case, between $\mathrm{Ra} = 10^4$ and $\mathrm{Ra} = 3 \times 10^4$, the kinetic energy in the cavity is higher than in the no-radiation case. This is mainly due to an increase of potential energy in the radiation case. This will be discussed in details in Sec. 4. As the convection starts, the center of the cavity becomes more isothermal, but the temperature profile is steeper in the radiation case. Let us consider the lower half of the cavity: near the wall, the fluid is hotter than in the nearly isothermal center of the cavity. Therefore, the gas is emitting near the wall and then is absorbing up to the cavity center, creating a hump in the radiative power distribution, which is absent without convection. Because of the S_{x_3} symmetry, it is the exact opposite in the upper half of the cavity.

3.2. Higher Rayleigh numbers: unsteady convection

The onset of unsteadiness in the flow field occurs at different Rayleigh numbers, depending on the presence of radiation or not (between $\mathrm{Ra} = 10^5$

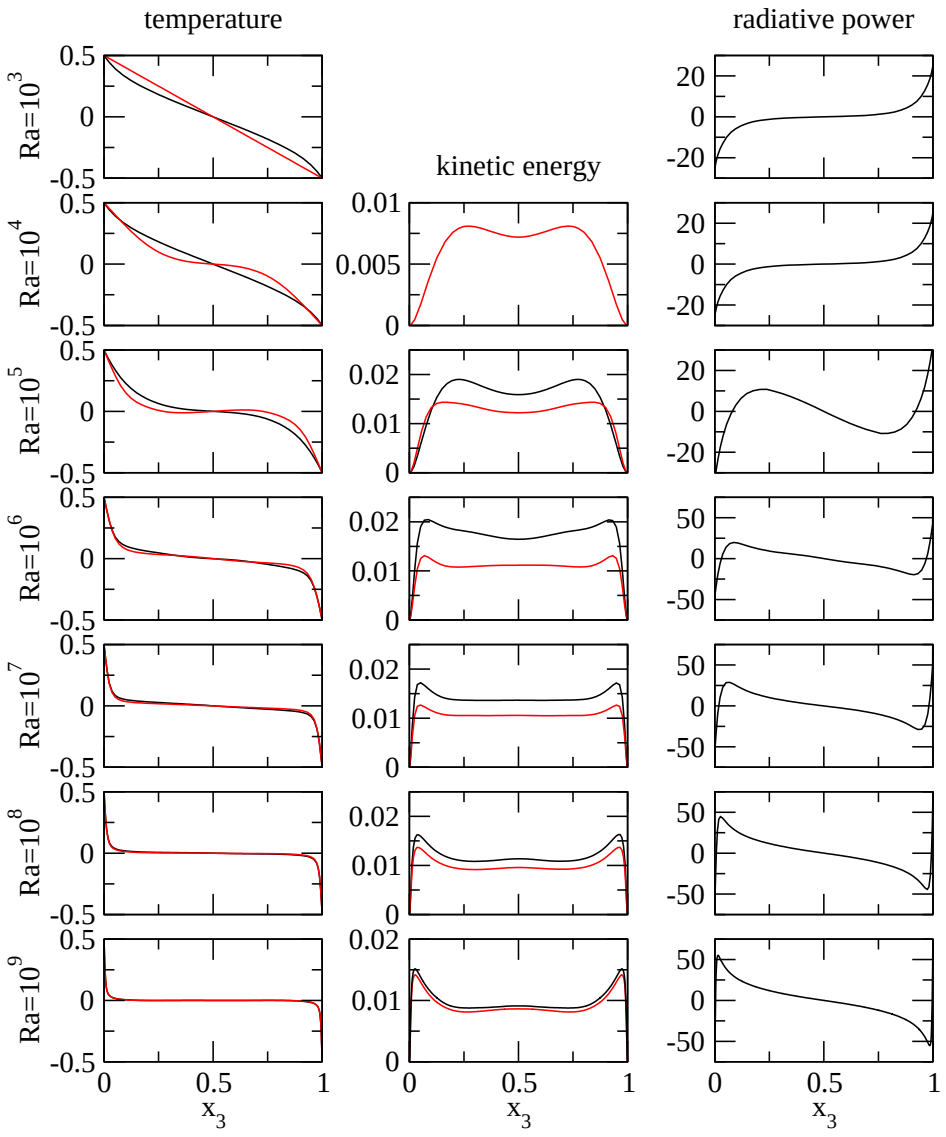

Figure 2: Flow fields at different Rayleigh numbers. Temperature, kinetic energy and radiative power, averaged over the horizontal plane and statistically averaged. Radiation case (black lines) and no-radiation case (red lines).

and $\mathrm{Ra} = 3 \times 10^5$ for the no-radiation case, and between $\mathrm{Ra} = 3 \times 10^5$ and $\mathrm{Ra} = 10^6$ for the radiation case). Radiation seems to delay the onset of unsteadiness, though a detailed investigation of the stability of all possible flow patterns would be required to confirm this point. As the Rayleigh number increases, the convection is more efficient at mixing the fluid. Therefore, the cavity is quasi-isothermal and thermal boundary layers form near the upper and lower walls. The kinetic energy is more and more homogeneous in the center, with peaks near the walls, where the temperature gradient is stronger. As before, the presence of gas radiation increases the kinetic energy, even if the relative effect of radiation diminishes as the Rayleigh number increases [33]. In the energy budget, the radiative power roughly scales as

$$\frac{1}{\sqrt{\mathrm{Ra}}}\mathcal{P}_{\mathrm{rad}} = \mathcal{O}\left(\frac{1}{\sqrt{\mathrm{Ra}}}\frac{\kappa_P \sigma T_0^3 L^2}{\lambda}\right) \tag{15}$$

where $\kappa_P = \int \kappa_\nu I_\nu^0(T_0) d\nu \times \pi/(\sigma T_0^4)$ is the Planck mean absorption coefficient. Thus, the radiative power remains of the same order of magnitude but is penalized by the $1/\sqrt{\mathrm{Ra}}$ factor, whereas the order of magnitude of the convective term $\boldsymbol{u} \cdot \boldsymbol{\nabla}\theta$ remains the same regardless of the Rayleigh number.

In order to better show the thermal boundary layer in the range $10^7 \leqslant \mathrm{Ra} \leqslant 10^9$, Fig. 3 displays the temperature and radiative power distributions near the lower wall. Only the radiation case is shown as radiation has little effect on the boundary layer thickness for this Rayleigh number range. It can be seen that the thickness of the thermal boundary layer roughly scales as $\mathrm{Ra}^{-1/3}$, in agreement with literature results in turbulent regime [57, 58]. The radiative power profile is similar to the one described at $\mathrm{Ra} = 10^5$: in the lower half of the cavity, the gas is rather absorbing except in a thin layer near the lower hot wall where the gas is emitting (the opposite happens nearby the upper wall). As the Rayleigh number increases, the convection mixing is stronger, the temperature gradient at the wall is sharper and the radiative power gradient at the wall increases. The thickness of the emitting layer and the position of the absorption peak also roughly scale as $\mathrm{Ra}^{-1/3}$.

3.3. Heat fluxes

Figure 4 shows the three components of the total heat flux q_{tot}

$$q_{\mathrm{tot}} = \underbrace{-\frac{\partial \left\langle \overline{\theta} \right\rangle_s}{\partial z}}_{q_{\mathrm{cond}}} + \underbrace{\sqrt{Ra}\left\langle \overline{\theta u_3} \right\rangle_s}_{q_{\mathrm{conv}}} + \underbrace{\frac{L}{\lambda \Delta T}\left\langle \overline{\sum_k \int_{4\pi} I_k \boldsymbol{\Omega} \cdot \boldsymbol{e_{x_3}} d\boldsymbol{\Omega}} \right\rangle_s}_{q_{\mathrm{rad}}}, \tag{16}$$

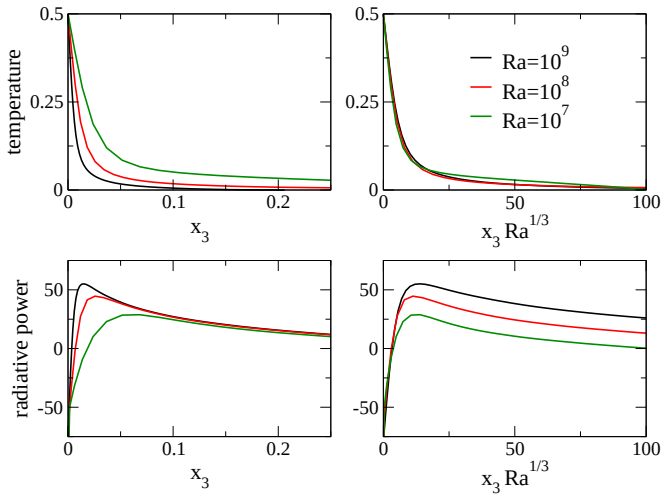

Figure 3: Temperature and radiative power close to the hot wall, averaged over the horizontal plane and statistically averaged. Rayleigh number range $10^7 \leqslant \mathrm{Ra} \leqslant 10^9$. Radiation case. On the right plots, the abscissa is scaled by $\mathrm{Ra}^{1/3}$.

where q_{cond}, q_{conv} and q_{rad} denote respectively the conductive, the convective and the radiative flux. $\langle\cdot\rangle_s$ denotes the spatial average over the horizontal plane and $\bar{\cdot}$ denotes the statistical average as defined in Eq. (14). The total flux q_{tot} is constant with height as the side walls are adiabatic. Values of wall fluxes and mid-height fluxes are reported in Tabs. 4 and 5 for the no-radiation case and the radiation case, respectively.

In the no-radiation case, there is a balance between the conductive and convective fluxes. The radiative flux, reported in Tab. 4, represents the energy exchange between the isothermal black upper and lower walls and is constant with height and across the range of Rayleigh numbers. Figure 4 shows that, at high Rayleigh numbers ($\mathrm{Ra} \geqslant 10^6$), variations of the conductive and convective fluxes are restricted to the boundary layer regions. In the center, convection prevails and conduction vanishes.

When gas radiation is taken into account, however, it modifies the balance between the fluxes. At low Rayleigh numbers, before the onset of convection in the cavity, the conduction-radiation coupling enables a greater conductive flux near the wall, as seen is Fig. 4. With the onset of convection, the presence of a radiating gas allows a greater convective flux in the center of the cavity: contrary to the no-radiation case, the variations of the convective

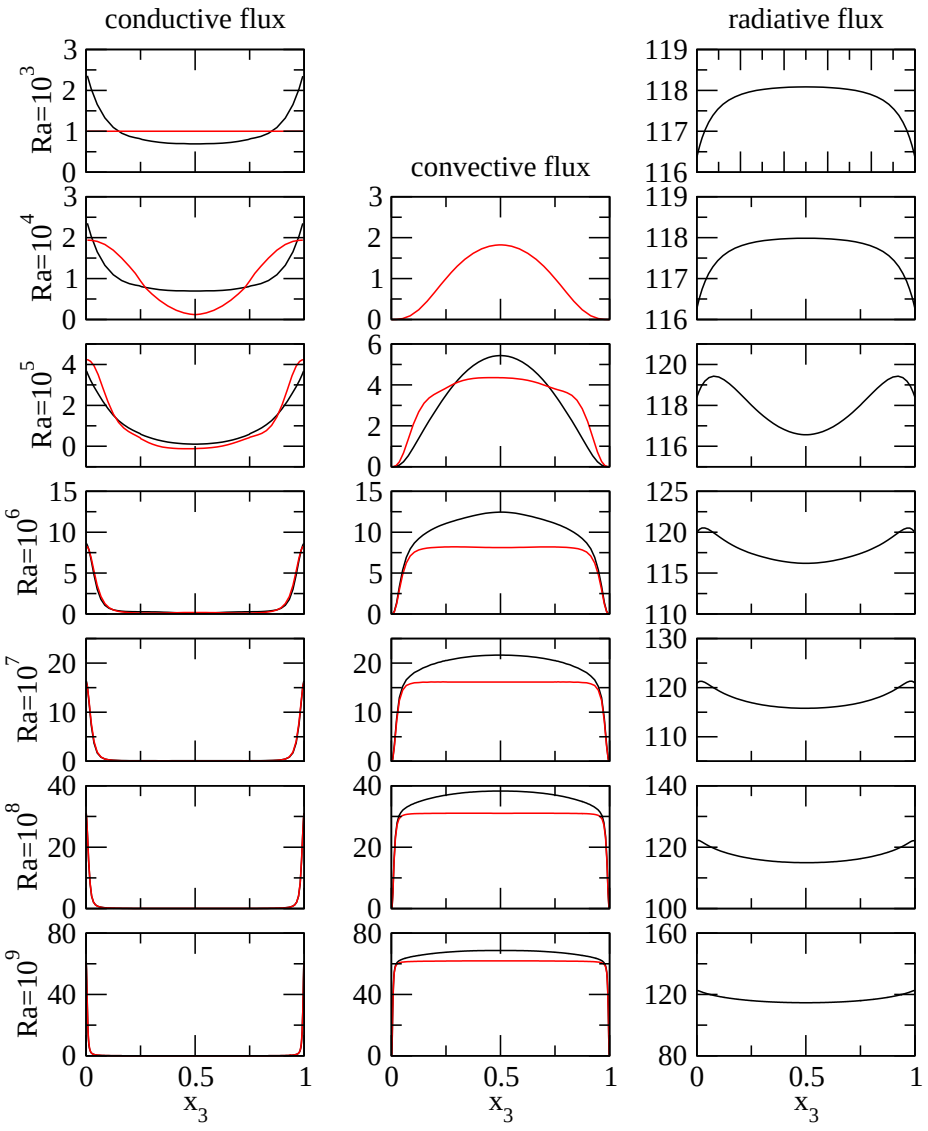

Figure 4: Heat fluxes at different Rayleigh numbers. Conductive flux, convective flux and radiative flux, averaged over the horizontal plane and statistically averaged. Radiation case (black lines) and no-radiation case (red lines).

	wall		mid-height		
Ra	q_{cond}	q_{rad}	q_{cond}	q_{conv}	q_{rad}
10^3	1.00	125.05	1.00	-	125.05
3×10^3	1.00	125.05	1.00	-	125.05
10^4	1.94	125.05	0.12	1.82	125.05
3×10^4	2.67	125.05	-0.13	2.80	125.05
10^5	4.24	125.05	-0.11	4.35	125.05
3×10^5	5.92	125.05	-0.06	5.99	125.05
10^6	8.30	125.05	0.18	8.12	125.05
3×10^6	11.48	125.05	0.15	11.34	125.05
10^7	16.24	125.05	0.08	16.14	125.05
3×10^7	22.06	125.05	0.04	22.02	125.05
10^8	31.06	125.05	0.02	31.04	125.05
10^9	61.38	125.05	0.002	61.87	125.05

Table 4: Wall heat fluxes and mid-height heat fluxes at different Rayleigh numbers. Conductive flux, convective flux and radiative flux, averaged over the horizontal plane and statistically averaged. No-radiation case.

	wall		mid-height		
Ra	q_{cond}	q_{rad}	q_{cond}	q_{conv}	q_{rad}
10^3	2.55	116.31	0.71	-	118.15
3×10^3	2.55	116.31	0.71	-	118.15
10^4	2.55	116.31	0.71	-	118.15
3×10^4	2,74	116.48	0.55	1.06	117.61
10^5	3.79	118.39	0.10	5.46	116.60
3×10^5	6.45	119.28	0.03	9.57	116.10
10^6	8.77	119.88	0.09	12.44	116.12
3×10^6	11.87	120.29	0.17	15.90	116.08
10^7	16.66	120.82	0.12	21.62	115.77
3×10^7	22.29	121.93	0.07	28.73	115.46
10^8	31.29	121.97	0.03	38.29	114.90
10^9	61.82	122.36	0.007	68.61	114.60

Table 5: Wall heat fluxes and mid-height heat fluxes at different Rayleigh numbers. Conductive flux, convective flux and radiative flux, averaged over the horizontal plane and statistically averaged. Radiation case.

flux are not restricted to the boundary layers due to a convection-radiation coupling in the quasi-isothermal part of the cavity. Though, the influence of radiative transfer decreases as the Rayleigh number increases, as seen in Eqs. (16): the convective flux scales as $\sqrt{\mathrm{Ra}}$, but not the radiative nor the conductive fluxes, whose relative effects become less important at higher Rayleigh numbers ($q_{\mathrm{rad}} = \mathcal{O}(\kappa_P \sigma T_0^3 L^2/\lambda)$, the cavity size L being constant). Comparing Tabs. 4 and 5, it can also be noticed that the radiative flux at the wall decreases in the radiation case (screening effect due to gas radiation) and that gas radiation has little effect on the conductive flux at the wall for $\mathrm{Ra} \geqslant 10^6$.

4. Energy budgets

We investigate in this section the effect of gas radiation on the balance of three quantities: the kinetic energy $e_k = \frac{1}{2}\overline{u_i u_i}$, the potential energy $e_p = -\mathrm{Pr}\overline{\theta}(x_3 - 0.5)$ and the *thermal energy* $e_\theta = \frac{1}{2}\overline{\theta^2}$, where $\bar{\cdot}$ denotes the statistical average as defined in Eq. (14). For the latter quantity e_θ, the word energy is used in a statistical sense and not in a physical sense and we use italics to emphasize it. The volume average of these three quantities at different Rayleigh numbers is shown in Fig. 5.

As stated in Sec. 3.1, gas radiation in the cavity delays the onset of convection: in the no-radiation case, the convection starts between $\mathrm{Ra} = 3 \times 10^3$ and $\mathrm{Ra} = 10^4$, whereas with gas radiation it starts between $\mathrm{Ra} = 10^4$ and $\mathrm{Ra} = 3 \times 10^4$. Kinetic energy increases with the Rayleigh number and reaches a peak at $\mathrm{Ra} = 3 \times 10^5$. In the no-radiation case, the kinetic energy remains quite constant across the unsteady regime. The velocity was made dimensionless using the reference velocity $u_{\mathrm{ref}} = \frac{a\sqrt{\mathrm{Ra}}}{L}$, which corresponds to a balance between the inertial and buoyancy forces. The quasi-plateau of the kinetic energy in the unsteady regime confirms that the reference velocity is well suited in this study. Gas radiation clearly increases the kinetic energy from $\mathrm{Ra} \geqslant 10^5$: the kinetic energy peak is almost 50% higher in the radiation case than in the no-radiation case. Like the fluxes, the relative effect of radiation is less important as the Rayleigh number increases and the kinetic energy then decreases and becomes closer to the no-radiation case.

Potential energy and *thermal energy* are related to differences between the local temperature of the fluid and the mean temperature in the cavity. Both decrease with the Rayleigh number, given that the boundary layer zones (with the highest temperature gradients) narrow. As stated in Sec. 3.1, before

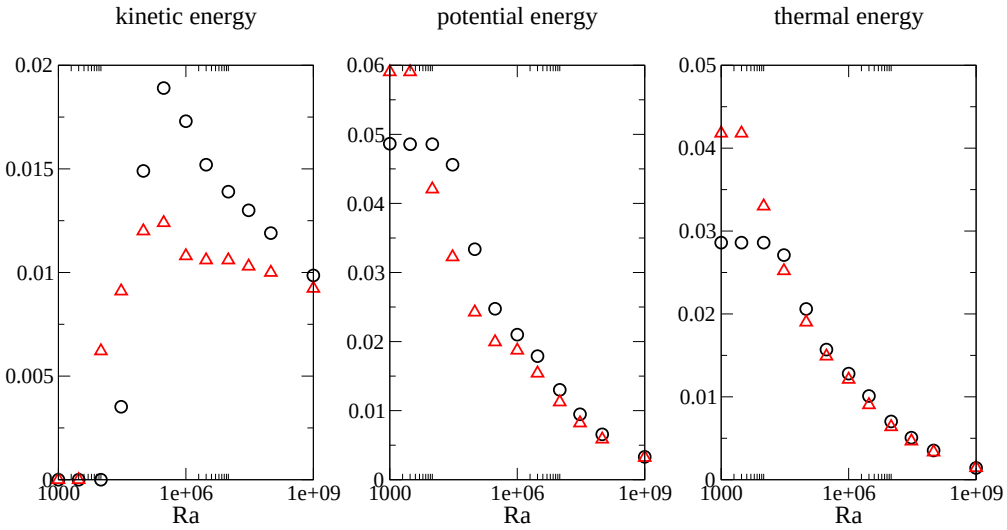

Figure 5: Total kinetic energy $\langle e_k \rangle_v$, potential energy $\langle e_p \rangle_v$ and *thermal energy* $\langle e_\theta \rangle_v$ as a function of the Rayleigh number. Radiation case (black symbols) and no-radiation case (red symbols).

the onset of convection, gas radiation decreases the temperature gradient in the core, and thus the potential energy and the *thermal energy*. However, after the onset, both are higher in the radiation case because of a higher temperature gradient in the core.

The kinetic energy balance can be written in the form

$$\frac{\partial e_k}{\partial t} + \frac{\partial u_j e_k}{\partial x_j} = -\frac{\partial u_i p}{\partial x_i} + \mathrm{Pr}\theta u_3 + \frac{\mathrm{Pr}}{\sqrt{\mathrm{Ra}}}\frac{\partial}{\partial x_j}\left(u_i \frac{\partial u_i}{\partial x_j}\right) - \frac{\mathrm{Pr}}{\sqrt{\mathrm{Ra}}}\frac{\partial u_i}{\partial x_j}\frac{\partial u_i}{\partial x_j}, \quad (17)$$

After applying volume average and statistical average, this equation writes

$$\underbrace{\mathrm{Pr}\left\langle \overline{\theta u_3} \right\rangle_v}_{\langle \tau_u \rangle_v} = \underbrace{\frac{\mathrm{Pr}}{\sqrt{\mathrm{Ra}}}\left\langle \overline{\frac{\partial u_i}{\partial x_j}\frac{\partial u_i}{\partial x_j}} \right\rangle_v}_{\langle \varepsilon_u \rangle_v}, \quad (18)$$

where $\langle \tau_u \rangle_v$ is the total production of kinetic energy (work of buoyant forces) and $\langle \varepsilon_u \rangle_v$ denotes the total mechanical dissipation. Radiation does not affect directly this balance.

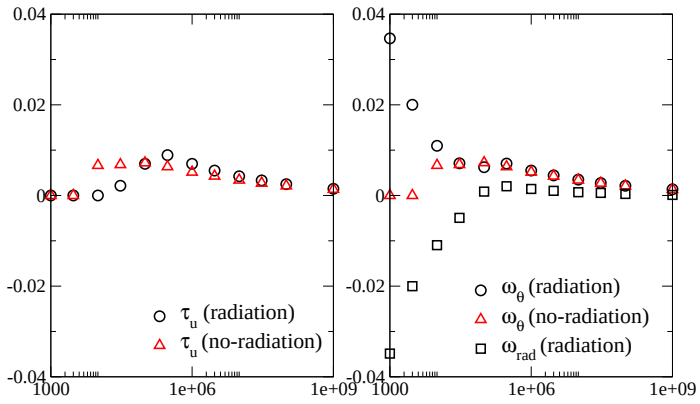

Figure 6: Potential energy balance: $\langle \tau_u \rangle_v$, $\langle \omega_\theta \rangle_v$ and $\langle \omega_{\rm rad} \rangle_v$ as a function of the Rayleigh number. Radiation case (black symbols) and no-radiation case (red symbols).

The potential energy balance writes

$$\frac{\partial e_p}{\partial t} + \frac{\partial u_j e_p}{\partial x_j} = -{\rm Pr}\theta u_3 - \frac{\rm Pr}{\sqrt{\rm Ra}} \frac{\partial}{\partial x_i}\left((x_3 - 0.5) \frac{\partial \theta}{\partial x_i} \right) + \frac{\rm Pr}{\sqrt{\rm Ra}} \frac{\partial \theta}{\partial x_3} - \frac{\rm Pr}{\sqrt{\rm Ra}} (x_3 - 0.5) \mathcal{P}_{\rm rad}. \quad (19)$$

After applying volume average and statistical average, this equation writes

$$\underbrace{\frac{\rm Pr}{\sqrt{\rm Ra}} ({\rm Nu} - 1)}_{\langle \omega_\theta \rangle_v} \underbrace{- \frac{\rm Pr}{\sqrt{\rm Ra}} \left\langle (x_3 - 0.5) \overline{\mathcal{P}_{\rm rad}} \right\rangle_v}_{\langle \omega_{\rm rad} \rangle_v} = \underbrace{{\rm Pr} \left\langle \overline{\theta u_3} \right\rangle_v}_{\langle \tau_u \rangle_v}, \quad (20)$$

where Nu is the Nusselt number (conductive flux at the wall). Terms $\langle \omega_\theta \rangle_v$ and $\langle \omega_{\rm rad} \rangle_v$ correspond to sources / sinks of potential energy associated with conduction and radiation transport of temperature variations. These sources / sinks are balanced with kinetic energy production ($\langle \tau_u \rangle_v$, see Eq. (18)). The three terms of the balance of Eq. (20) are displayed in Fig. 6.

At the lowest Rayleigh numbers, $\langle \tau_u \rangle_v = 0$ because there is no fluid movement, and thus Nu = 1 in the no-radiation case, which is consistent with the profile of the conductive flux in Fig. 4. However, the conductive

flux is sharper near the walls in the radiation case, even in the absence of convection (see 3.3). Thereby, the Nusselt number is greater than one and $\langle\omega_\theta\rangle_v$ is positive at low Rayleigh numbers. Interestingly the sign of the term $\langle\omega_{\rm rad}\rangle_v$ changes with the Rayleigh number: it is negative at low Rayleigh numbers and positive from $\mathrm{Ra} = 10^5$, when the kinetic energy is greater in the radiation case than in the no-radiation case. Therefore, the sign of this term determines whether gas radiation slows down convection or promotes convection. The sign change of $\langle\omega_{\rm rad}\rangle_v$ is correlated with the modification of the shape of the radiative power in Fig. 2. In the absence of convection, the lower half of the cavity ($x_3 < 0.5$) is exclusively emitting ($\mathcal{P}_{\rm rad} < 0$) and the upper half ($x_3 > 0.5$) is exclusively absorbing ($\mathcal{P}_{\rm rad} > 0$), which corresponds to a destruction of potential energy ($\langle\omega_{\rm rad}\rangle_v < 0$). With the onset of convection, the lower half becomes absorbing, except for a thin layer near the isothermal wall that is still emitting, and the opposite happens in the upper half: this corresponds to a production of potential energy ($\langle\omega_{\rm rad}\rangle_v > 0$).

The *thermal energy* balance writes

$$\frac{\partial e_\theta}{\partial t} + \frac{\partial u_j e_\theta}{\partial x_j} = \frac{1}{\sqrt{\mathrm{Ra}}}\frac{\partial}{\partial x_i}\left(\theta\frac{\partial\theta}{\partial x_i}\right) - \frac{1}{\sqrt{\mathrm{Ra}}}\frac{\partial\theta}{\partial x_i}\frac{\partial\theta}{\partial x_i} + \frac{1}{\sqrt{\mathrm{Ra}}}\theta\mathcal{P}_{\rm rad}. \tag{21}$$

After applying volume average and statistical average, this equation writes

$$\underbrace{\frac{\mathrm{Nu}}{\sqrt{\mathrm{Ra}}}}_{\langle\tau_\theta\rangle_v} = \underbrace{\frac{1}{\sqrt{\mathrm{Ra}}}\left\langle\overline{\frac{\partial\theta}{\partial x_i}\frac{\partial\theta}{\partial x_i}}\right\rangle_v}_{\langle\varepsilon_\theta\rangle_v} \underbrace{-\frac{1}{\sqrt{\mathrm{Ra}}}\left\langle\overline{\theta\mathcal{P}_{\rm rad}}\right\rangle_v}_{\langle\varepsilon_{\rm rad}\rangle_v}. \tag{22}$$

The production of *thermal energy* ($\langle\tau_\theta\rangle_v$) is dissipated through two mechanisms: conduction ($\langle\varepsilon_\theta\rangle_v$) and radiation ($\langle\varepsilon_{\rm rad}\rangle_v$). The three terms of the balance of Eq. (22) are displayed in Fig. 7.

At the lowest Rayleigh numbers, the production of *thermal energy* is much higher in the radiation case than in the no-radiation one, due to significant differences in conductive fluxes. The dissipation distributes quite evenly between conduction and radiation until the onset of convection, where the importance of radiation reduces compared to conduction. At higher Rayleigh numbers, the radiative dissipation is negligible.

5. Turbulence budgets

We analyse in this section turbulence budgets of velocity and temperature fluctuating fields in the range $10^7 \leqslant \mathrm{Ra} \leqslant 10^9$. Mean and fluctuating fields

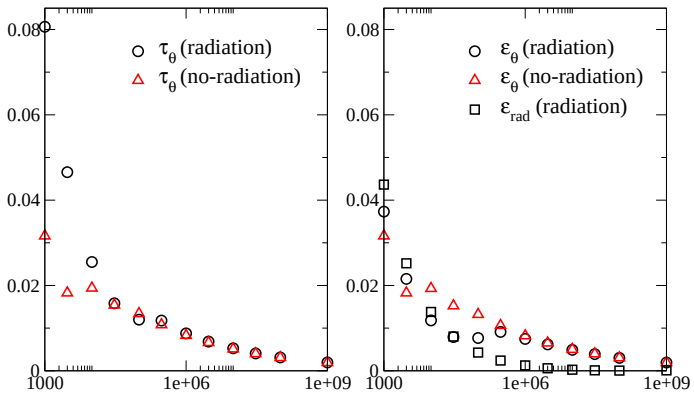

Figure 7: *Thermal energy* balance: $\langle \tau_\theta \rangle_v$, $\langle \varepsilon_\theta \rangle_v$ and $\langle \varepsilon_{\rm rad} \rangle_v$ as a function of the Rayleigh number. Radiation case (black symbols) and no-radiation case (red symbols).

are defined according to the statistical average $\overline{\cdot}$ given by Eq. (14). Details on the computation of second order and third order statistics with this statistical mean are given in Appendix A.

The turbulent kinetic energy balance $\overline{e_k(\boldsymbol{u}')} = \frac{1}{2}\overline{u_i' u_i'}$ writes

$$\frac{\partial \overline{e_k(\boldsymbol{u}')}}{\partial t} + \overline{u_j}\frac{\partial \overline{e_k(\boldsymbol{u}')}}{\partial x_j} = \underbrace{-\frac{\partial}{\partial x_j}\left(\overline{u_j' p'} + \frac{1}{2}\overline{u_i' u_i' u_j'} - \frac{\mathrm{Pr}}{\sqrt{\mathrm{Ra}}}\frac{\partial \overline{e_k(\boldsymbol{u}')}}{\partial x_j}\right)}_{\delta_{u'}}$$

$$\underbrace{+\mathrm{Pr}\overline{u_3'\theta'}}_{\tau_{u'}} \underbrace{-\overline{u_i' u_j'}\frac{\partial \overline{u_i}}{\partial x_j}}_{\zeta_{u'}} \underbrace{-\frac{\mathrm{Pr}}{\sqrt{\mathrm{Ra}}}\overline{\frac{\partial u_i'}{\partial x_j}\frac{\partial u_i'}{\partial x_j}}}_{-\varepsilon_{u'}}. \quad (23)$$

In the above equation, $\tau_{u'}$ is the production term of turbulent kinetic energy by the work of buoyancy forces, $\zeta_{u'}$, is an energy exchange term between mean and fluctuating flow, $\varepsilon_{u'}$ is the molecular dissipation term (always positive), while $\delta_{u'}$ appears as a diffusion term — which vanishes when integrating over the whole spatial domain for non slip boundary conditions. Table 6 provides these volume integrated production ($\langle \tau_{u'} \rangle_v$), transfer ($\langle \zeta_{u'} \rangle_v$), and dissipation ($\langle \varepsilon_{u'} \rangle_v$) terms, in the radiation and no-radiation cases for the three Rayleigh numbers 10^7, 10^8, and 10^9. In the six considered configurations, the

Ra	10^7		10^8		10^9	
terms $\times 10^3$	no-rad	rad	no-rad	rad	no-rad	rad
$\langle \tau_{u'} \rangle_v$	2.65	3.45 (30%)	1.77	2.09 (18%)	1.19	1.29 (8%)
$\langle \zeta_{u'} \rangle_v$	0.27	0.27 (——)	0.18	0.20 (13%)	0.10	0.11 (8%)
$\langle \varepsilon_{u'} \rangle_v$	2.96	3.87 (31%)	2.02	2.50 (24%)	1.43	1.56 (9%)

Table 6: Production $\langle \tau_{u'} \rangle_v$, transfer $\langle \zeta_{u'} \rangle_v$, and dissipation $\langle \varepsilon_{u'} \rangle_v$ terms of the turbulent kinetic energy balance, averaged on the whole domain, in the radiation (rad) and no-radiation (no-rad) cases for the three Rayleigh numbers Ra= 10^7, 10^8, and 10^9. Term variations due to radiation are provided in parentheses

integrated production term $\langle \tau_{u'} \rangle_v$ highly dominates the transfer term $\langle \zeta_{u'} \rangle_v$ (by a factor ~ 10) contrary to what was observed in differentially heated configurations [33]. Radiation always increases this production term (and also the dissipation one necessarily), the magnitude of the increase being reduced when the Rayleigh number increases. This increase is consistent with the convection enhancement in the radiation case discussed in the previous sections.

Figure 8 shows the vertical distribution of each term in the right hand side of Eq. (23), averaged over the horizontal plane. Contrary to volume integrated terms, all terms can significantly contribute to the local balance of turbulent kinetic energy. In addition, all sources of mechanical fluctuations are significant in the core of the cavity which means the dynamics of turbulent fluctuations is not restricted to the boundary layers near the hot and cold walls. Note that the transfer term like the diffusion one have a varying sign through all the domain, which explains that they can contribute significantly to the local balance and in a much lesser extent to the global balance. Interestingly, the transfer term is negative in the boundary layer, while the mean flow shear at the walls is usually a source of turbulent fluctuations in most flows.

The balance of the variance of temperature fluctuations $\overline{e_\theta(\theta')} = \frac{1}{2}\overline{\theta'\theta'}$

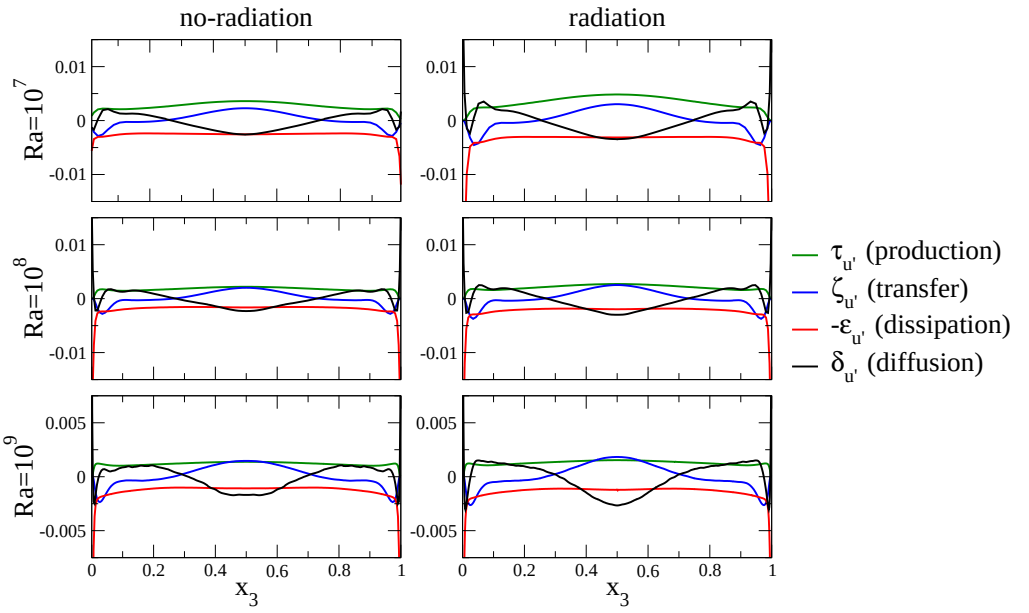

Figure 8: Turbulent kinetic energy budget in the range $10^7 \leq Ra \leq 10^9$. Production $\tau_{u'}$ (green lines), transfer $\zeta_{u'}$ (blue lines), dissipation $\varepsilon_{u'}$ (red lines) and diffusion $\delta_{u'}$ (black lines) of turbulent kinetic energy for radiation and no-radiation cases.

writes

$$\frac{\partial \overline{e_\theta(\theta')}}{\partial t} + \overline{u_j}\frac{\partial \overline{e_\theta(\theta')}}{\partial x_j} = \underbrace{-\frac{\partial}{\partial x_j}\left(\frac{1}{2}\overline{u_j'\theta'\theta'} - \frac{1}{\sqrt{\mathrm{Ra}}}\frac{\partial \overline{e_\theta(\theta')}}{\partial x_j}\right)}_{\delta_{\theta'}} \underbrace{-\overline{u_j'\theta'}\frac{\partial \overline{\theta}}{\partial x_j}}_{\zeta_{\theta'}} \underbrace{-\frac{1}{\sqrt{\mathrm{Ra}}}\overline{\frac{\partial \theta'}{\partial x_j}\frac{\partial \theta'}{\partial x_j}}}_{-\varepsilon_{\theta'}} \underbrace{-\frac{1}{\sqrt{\mathrm{Ra}}}\overline{\theta'\mathcal{P}_{\mathrm{rad}}'}}_{-\varepsilon_{\mathrm{rad}'}} \quad (24)$$

Here again appear a diffusion term $\delta_{\theta'}$ and a transfer term $\zeta_{\theta'}$ between the mean temperature field and the fluctuating temperature field. $\varepsilon_{\theta'}$ corresponds to the conductive dissipation term. In the case of a radiating mixture, a supplementary radiative dissipation term $\varepsilon_{\mathrm{rad}'}$ appears. After integration over the whole spatial domain, this balance of temperature fluctuation variance reduces to an equilibrium between the transfer source term $\langle \zeta_{\theta'} \rangle_v$, and the conductive $\langle \varepsilon_{\theta'} \rangle_v$ and radiative (if relevant) $\langle \varepsilon_{\mathrm{rad}'} \rangle_v$ dissipation terms — the contribution of the diffusion term vanishes since temperature fluctuations at isothermal horizontal walls and temperature gradients at adiabatic perfectly reflecting walls vanish. Table 7 provides these volume integrated terms in the radiation and no-radiation cases for the three Rayleigh numbers 10^7, 10^8, and 10^9. Here again, radiation is shown to increase the transfer term, but to a lesser extent compared to the increase observed for velocity fluctuations. The radiative dissipation term contributes to 10% of the transfer term at Ra=10^7 but reduces to 5 and 1% at Ra =10^8 and 10^9 respectively. This behaviour was already observed in differentially heated configurations [33] and was explained by the ability of radiative transfer to dissipate large scale thermal structures while conduction becomes more efficient for smaller scale structures that occur at higher Rayleigh numbers [59].

Figure 9 shows the vertical distribution of each term in the right hand side of Eq. (24), averaged over the horizontal plane. There is a slight increase of each term when radiation is taken into account, as observed above on volume integrated terms: this is particularly noticeable at $Ra = 10^7$. Let note again that the diffusion term, though vanishing in volume integrated balances, may have a significant local contribution in the redistribution of temperature fluctuations, in particular in the boundary layers near horizontal hot and cold walls. Contrary to mechanical fluctuations, the transfer term is positive in the boundary layers and the dynamics of fluctuations in the core

Ra	10^7		10^8		10^9	
terms $\times 10^3$	no-rad	rad	no-rad	rad	no-rad	rad
$\langle \zeta_{\theta'} \rangle_v$	1.73	1.99 (15%)	1.16	1.23 (6%)	0.774	0.780 (1%)
$\langle \varepsilon_{\theta'} \rangle_v$	1.73	1.81 (5%)	1.16	1.23 (6%)	0.797	0.797 (—-)
$\langle \varepsilon_{\mathrm{rad}'} \rangle_v$	—	0.20	—	0.06	—	0.008

Table 7: Transfer $\langle \zeta_{\theta'} \rangle_v$, conductive $\langle \varepsilon_{\theta'} \rangle_v$ and radiative $\langle \varepsilon_{\mathrm{rad}'} \rangle_v$ dissipation terms of the balance equation for the variance of temperature fluctuations, averaged on the whole domain, in the radiative (rad) and non-radiative (no-rad) cases for the three Rayleigh numbers Ra= 10^7, 10^8, and 10^9.

is very weak.

6. Conclusion

Direct numerical simulations of Rayleigh-Bénard convection in a cubic cell for a radiating air-H_2O-CO_2 mixture have been performed over a large range of Rayleigh numbers ($\mathrm{Ra} \in [10^3 - 10^9]$), from the onset of convection to the turbulent regime.

At low Rayleigh numbers, conduction-radiation energy exchanges make the temperature field more stable. This coupling delays the onset of convection. Once convection settles, convection-radiation exchanges in the cavity core have been highlighted. When gas radiation is taken into account energy transfer is no longer restricted to the boundary layers: convection is enhanced and so is the total kinetic energy of the flow. Gas radiation also increases the conductive flux and decreases the radiative flux at the two opaque isothermal walls, though differences with the no-radiation case are below 5 % from $\mathrm{Ra} \geqslant 10^6$. Because the Rayleigh number is varied through the temperature difference ΔT, radiative transfer effects weaken when the Rayleigh number increases.

Specific contributions of radiative transfer to the potential energy balance and the *thermal energy* balance have been highlighted. It has been shown that gas radiation acts as a sink of potential energy at low Rayleigh numbers and as a source of potential energy from $\mathrm{Ra} \geqslant 10^5$. In the *thermal energy* balance, radiation effects correspond to a dissipation of temperature differences. This radiative dissipation is comparable to the conductive dissipation up to $\mathrm{Ra} = 10^5$, but decreases and becomes negligible for higher Rayleigh numbers.

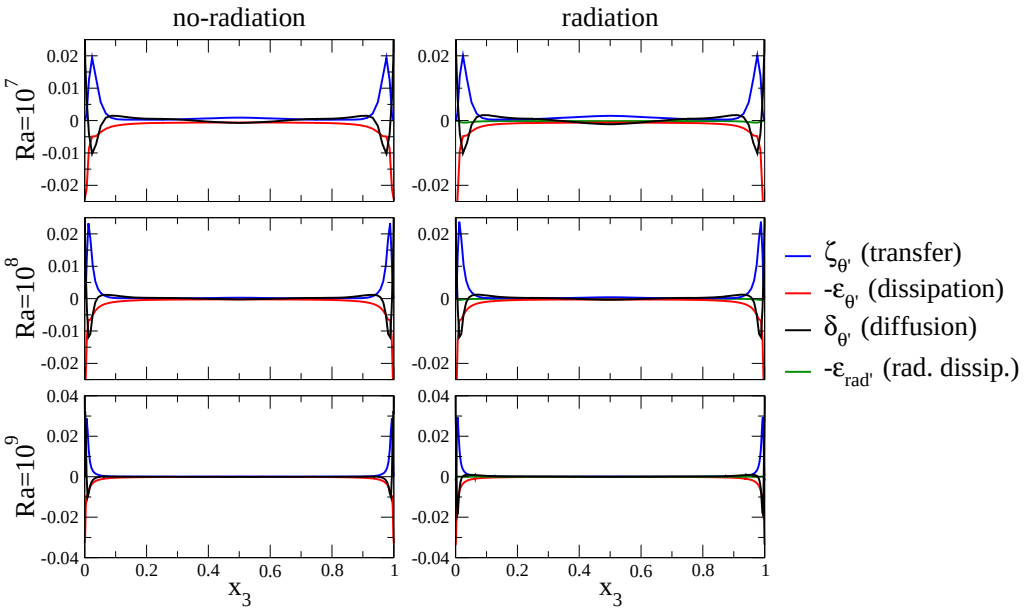

Figure 9: Budget of temperature variance in the range $10^7 \leq Ra \leq 10^9$. Transfer $\zeta_{\theta'}$ (blue lines), dissipation $\varepsilon_{\theta'}$ (red lines), diffusion $\delta_{\theta'}$ (black lines) and radiative dissipation $\varepsilon_{\mathrm{rad}'}$ (green lines) of temperature variance for radiation and no-radiation cases.

At high Rayleigh numbers, in the range $10^7 \leqslant \mathrm{Ra} \leqslant 10^9$, the analysis of turbulence statistics has shown that all sources of turbulent fluctuations are stronger in the radiation case, especially velocity fluctuations. This turbulence intensification is associated with the convection enhancement observed when gas radiation is accounted for. Sources of temperature fluctuations are less affected by gas radiation: the convection enhancement is mitigated by radiative dissipation of temperature disturbances, although this term remains weak compared to other sources. Again, radiation effects on turbulence statistics weaken when the Rayleigh number increases.

To the best of our knowledge, the present coupled simulations are the first to address Rayleigh-Bénard convection of a radiating gas at such high Rayleigh numbers and such wide Rayleigh number range. Results will be useful for the development and validation of reduced order models or large-eddy simulation models, accounting for radiation effects. However, the simulations were restricted to a single gas mixture and a single cavity size. Sensitivity of radiation effects on these parameters will be the topic of future research.

Acknowledgements

This work benefited from the financial support of the "Agence de l'environnement et de la maîtrise de l'énergie" (ADEME, France). This work was granted access to the HPC resources of IDRIS under the allocation 2020-A0062B00209 attributed by GENCI (Grand Equipement National de Calcul Intensif). This work was also performed using HPC resources from the Mésocentre computing center of CentraleSupélec and École Normale Supérieure Paris-Saclay supported by CNRS and Région Île-de-France (http://mesocentre.centralesupelec.fr/).

Appendix A. Turbulence statistics using symmetry average

This section details the computation of second order and third order turbulence statistics in turbulence budgets of Sec. 5 with the statistical average defined in Eq. (14), which implies an ensemble average of symmetrised time evolutions of each flow variable of interest.

The first step is to compute the symmetry average (ensemble average over symmetrised states) of physical quantities of the form ϕ, $\phi\psi$ or $\phi\phi\psi$. To do this, we need to express the action of each elementary symmetry S_{x_1}, S_{x_2}, S_{x_3} and S_d (Eqs. (10)-(13)) on each flow variable and each product of flow variables of interest. This is given in Tab. A.8. Note that for third

(x_1, x_2, x_3)	S_{x_1} $(1-x_1, x_2, x_3)$	S_{x_2} $(x_1, 1-x_2, x_3)$	S_{x_3} $(x_1, x_2, 1-x_3)$	S_d (x_2, x_1, x_3)
u_1	$-u_1$	u_1	u_1	u_2
u_2	u_2	$-u_2$	u_2	u_1
u_3	u_3	u_3	$-u_3$	u_3
θ	θ	θ	$-\theta$	θ
$\mathcal{P}_{\text{rad}}$	$\mathcal{P}_{\text{rad}}$	$\mathcal{P}_{\text{rad}}$	$-\mathcal{P}_{\text{rad}}$	$\mathcal{P}_{\text{rad}}$
u_1u_1	u_1u_1	u_1u_1	u_1u_1	u_2u_2
u_1u_2	$-u_1u_2$	$-u_1u_2$	u_1u_2	u_1u_2
u_1u_3	$-u_1u_3$	u_1u_3	$-u_1u_3$	u_2u_3
u_2u_2	u_2u_2	u_2u_2	u_2u_2	u_1u_1
u_2u_3	u_2u_3	$-u_2u_3$	$-u_2u_3$	u_1u_3
u_3u_3	u_3u_3	u_3u_3	u_3u_3	u_3u_3
$\theta\theta$	$\theta\theta$	$\theta\theta$	$\theta\theta$	$\theta\theta$
$u_1\theta$	$-u_1\theta$	$u_1\theta$	$-u_1\theta$	$u_2\theta$
$u_2\theta$	$u_2\theta$	$-u_2\theta$	$-u_2\theta$	$u_1\theta$
$u_3\theta$	$u_3\theta$	$u_3\theta$	$u_3\theta$	$u_3\theta$
ε_u	ε_u	ε_u	ε_u	ε_u
ε_θ	ε_θ	ε_θ	ε_θ	ε_θ
ε_{rad}	ε_{rad}	ε_{rad}	ε_{rad}	ε_{rad}
$u_1u_1u_3$	$u_1u_1u_3$	$u_1u_1u_3$	$-u_1u_1u_3$	$u_2u_2u_3$
$u_2u_2u_3$	$u_2u_2u_3$	$u_2u_2u_3$	$-u_2u_2u_3$	$u_1u_1u_3$
$u_3u_3u_3$	$u_3u_3u_3$	$u_3u_3u_3$	$-u_3u_3u_3$	$u_3u_3u_3$
$\theta\theta u_3$	$\theta\theta u_3$	$\theta\theta u_3$	$-\theta\theta u_3$	$\theta\theta u_3$

Table A.8: Action of elementary symmetries defined in Eqs. (10)-(13)) on each flow variable or product of flow variable of interest.

order statistics, only products of the type $\phi\phi u_3$ are required to compute the diffusion terms $\delta_{u'}$ and $\delta_{\theta'}$ in Eqs. (23)-(24), averaged over horizontal planes. The symmetry average can be applied before the time average or after the time average, indifferently.

Once averaged quantities $\overline{\phi}$, $\overline{\phi\psi}$ or $\overline{\phi\phi\psi}$ are known, the second step consists in computing second order statistics $\overline{\phi'\psi'}$ or third order statistics $\overline{\phi'\phi'\psi'}$ with the following relationships

$$\overline{\phi'\psi'} = \overline{\phi\psi} - \overline{\phi}\,\overline{\psi}, \tag{A.1}$$

$$\overline{\phi'\phi'\psi'} = \overline{\phi\phi\psi} - \overline{\phi}\,\overline{\phi}\,\overline{\psi} - 2\overline{\phi'\psi'}\,\overline{\phi} - \overline{\phi'\phi'}\,\overline{\psi}. \tag{A.2}$$

References

[1] S. Chandrasekhar, Hydrodynamic and Hydromagnetic Stability, Dover, New York, 1981.

[2] J. Pallares, F. Grau, F. Giralt, Flow transitions in laminar Rayleigh-Bénard convection in a cubical cavity at moderate Rayleigh numbers , International Journal of Heat and Mass Transfer 42 (4) (1999) 753 – 769.

[3] D. Puigjaner, J. Herrero, F. Giralt, C. Simó, Stability analysis of the flow in a cubical cavity heated from below, Physics of Fluids 16 (10) (2004) 3639.

[4] F. Bousset, D. Lyubimov, G. Sedel'nikov, Three-dimensional convection regimes in a cubical cavity, Fluid Dynamics 43 (1) (2008) 1–8.

[5] D. Puigjaner, J. Herrero, C. Simó, F. Giralt, Bifurcation analysis of steady Rayleigh-Bénard convection in a cubical cavity with conducting sidewalls, Journal of Fluid Mechanics 598 (2008) 393–427.

[6] W. Leong, K. Hollands, A. Brunger, Experimental Nusselt numbers for a cubical-cavity benchmark problem in natural convection, International Journal of Heat and Mass Transfer 42 (11) (1999) 1979–1989.

[7] D. W. Pepper, K. G. T. Hollands, Summary of benchmark numerical studies for 3-D natural convection in an air-filled enclosure, Numerical Heat Transfer, Part A: Applications 42 (1-2) (2002) 1–11.

[8] K. R. Sreenivasan, A. Bershadski, J. J. Niemela, Mean wind and its reversal in thermal convection, Physical Review E 65 (056306) (2002).

[9] E. Brown, A. Nikolaenko, G. Ahlers, Reorientation of the large-scale circulation in turbulent Rayleigh-Bénard convection, Physical Review Letters 95 (2005) 084503.

[10] R. Benzi, R. Verzicco, Numerical simulations of flow reversal in Rayleigh-Bénard convection, Europhysics Letters 80 (64008) (2008).

[11] P. K. Mishra, A. K. De, M. K. Verma, V. Eswaran, Dynamics of reorientations and reversals of large-scale flow in Rayleigh-Bénard convection, Journal of Fluid Mechanics 668 (2011) 480–499.

[12] Y. Wang, P.-Y. Lai, H. Song, P. Tong, Mechanism of large-scale flow reversals in turbulent thermal convection, Science Advances 4 (2018) eaat7480.

[13] A. Xu, H.-D. Xi, Tristable flow states and reversal of the large-scale circulation in two-dimensional circular convection cells, Journal of Fluid Mechanics 910 (2021) A33–1.

[14] A. Vasiliev, A. Sukhanovskii, P. Frick, A. Budnikov, V. Fomichev, M. Bolshukhin, R. Romanov, High Rayleigh number convection in a cubic cell with adiabatic sidewalls, International Journal of Heat and Mass Transfer 102 (2016) 201–212.

[15] N. Foroozani, J. J. Niemela, V. Armenio, K. R. Sreenivasan, Reorientations of the large-scale flow in turbulent convection in a cube, Physical Review E 95 (2017) 033107.

[16] F. F. Araujo, S. Grossmann, D. Lohse, Wind reversals in turbulent Rayleigh-Bénard convection, Physical Review Letters 95 (2005) 084502.

[17] E. Brown, G. Ahlers, Large-scale circulation model for turbulent Rayleigh-Bénard convection, Physical Review Letters 98 (2007) 134501.

[18] E. Brown, G. Ahlers, Azimuthal asymmetries of the large-scale circulation in turbulent Rayleigh-Bénard convection, Physics of Fluids 20 (2008) 105105.

[19] K. Bai, D. Ji, E. Brown, Ability of a low-dimensional model to predict geometry-dependent dynamics of large-scale coherent structures in turbulence, Physical Review E 93 (2016) 023117.

[20] D. Ji, E. Brown, Low-dimensional model of the large-scale circulation of turbulent Rayleigh-Bénard convection in a cubic container, Physical Review Fluids 5 (2020) 064606.

[21] J. Bailon-Cuba, M. S. Emran, J. Schumacher, Aspect ratio dependence of heat transfer and large-scale flow in turbulent convection, Journal of Fluid Mechanics 655 (2010) 152–173.

[22] M. Chandra, M. K. Verma, Dynamics and symmetries of flow reversals in turbulent convection, Physical Review E 83 (2011) 067303.

[23] D. Giannakis, A. Kolchinskaya, D. Krasnov, J. Schumacher, Koopman analysis of the long-term evolution in a turbulent convection cell, Journal of Fluid Mechanics 847 (2018) 735–767.

[24] L. Soucasse, B. Podvin, Ph. Rivière, A. Soufiani, Proper orthogonal decomposition analysis and modelling of large-scale flow reorientations in a cubic Rayleigh-Bénard cell, Journal of Fluid Mechanics 881 (2019) 23–50.

[25] A. Xu, X. Chen, F. Wang, H.-D. Xi, Correlation of internal flow structure with heat transfer efficiency in turbulent Rayleigh–Bénard convection, Physics of Fluids 32 (2020) 105112.

[26] E. A. Spiegel, The smoothing of temperature fluctuations by radiative transfer, Astrophysical Journal 126 (1957) 202–207.

[27] E. A. Spiegel, The convective instability of a radiating fluid layer, Astrophysical Journal 132 (1960) 716–728.

[28] J. Gille, R. Goody, Convection in a radiating gas, Journal of Fluid Mechanics 20 (1964) 47–79.

[29] F. Bdéoui, A. Soufiani, The onset of Rayleigh–Bénard instability in molecular radiating gases, Physics of Fluids 9 (1997) 3858–3872.

[30] Bdéoui, F and Soufiani, A, and Le Quéré P., A numerical study of Rayleigh-Bénard convection in radiating gases, in: Proc. of 11th International Heat Transfer Conference, pp. 261-266, Taylor and Francis, 1998.

[31] C. H. Lan, O. A. Ezekoye, J. R. Howell, K. S. Ball, Stability analysis for three-dimensional Rayleigh–Bénard convection with radiatively participating medium using spectral methods, International Journal of Heat and Mass Transfer 46 (2003) 1371–1383.

[32] L. Soucasse, Ph. Rivière, A. Soufiani, S. Xin, P. Le Quéré, Transitional regimes of natural convection in a differentially heated cavity under the effects of wall and molecular gas radiation, Physics of Fluids 26 (2014) 024105.

[33] L. Soucasse, Ph. Rivière, A. Soufiani, Natural convection in a differentially heated cubical cavity under the effects of wall and molecular gas radiation at Rayleigh numbers up to $3\times$ 10^9, International Journal of Heat and Fluid Flow 61-B (2016) 510–530.

[34] T. Kogawa, J. Okajima, A. Sakurai, A. Komiya, S. Maruyama, Influence of radiation effect on turbulent natural convection in cubic cavity at normal temperature atmospheric gas, International Journal of Heat and Mass Transfer 104 (2017) 456–466.

[35] T. Kogawa, E. Shoji, J. Okajima, A. Komiya, S. Maruyama, Experimental evaluation of thermal radiation effects on natural convection with a Rayleigh number of 10^8-10^9 by using an interferometer, International Journal of Heat and Mass Transfer 132 (2019) 1239–1249.

[36] A. Sakurai, R. Kanbayashi, K. Matsubara, S. Maruyama, Radiative heat transfer analysis in a turbulent natural convection obtained from direct numerical simulation, Journal of Thermal Science and Technology 6 (3) (2011) 449–462.

[37] A. Sakurai, K. Matsubara, K. Takakuwa, R. Kanbayashi, Radiation effects on mixed turbulent natural and forced convection in a horizontal channel using direct numerical simulation, International Journal of Heat and Mass Transfer 55 (2012) 2539–2548.

[38] L. Soucasse, Ph. Rivière, A. Soufiani, Effects of molecular gas radiation on Rayleigh-Bénard convection in a 3D cubical cavity, in: Proceedings of the 15th International Heat Transfer Conference, 2014, pp. IHTC15–9563.

[39] L. Soucasse, B. Podvin, Ph. Rivière, A. Soufiani, Reduced-order modelling of radiative transfer effects on Rayleigh-Bénard convection in a cubic cell, Journal of Fluid Mechanics 898 (2020) A2.

[40] L. Soucasse, B. Podvin, Ph. Rivière, A. Soufiani, Low-order models for predicting radiative transfer effects on Rayleigh-Bénard convection in a cubic cell at different rayleigh numbers, submitted to Journal of Fluid Mechanics 917 (2021) A5.

[41] A. Sameen, R. Verzicco, K. R. Sreenivasan, Specific roles of fluid properties in non-Boussinesq thermal convection at the Rayleigh number of 2×10^8, Europhysics Letters 86 (2009) 14006.

[42] L. Pierrot, P. Rivière, A. Soufiani, J. Taine, A fictitious-gas-based absorption distribution function global model for radiative transfer in hot gases, Journal of Quantitative Spectroscopy and Radiative Transfer 62 (1999) 609–624.

[43] L. Soucasse, Ph. Rivière, S. Xin, P. Le Quéré, A. Soufiani, Numerical study of coupled molecular gas radiation and natural convection in a differentially heated cubical cavity, Computational Thermal Sciences 4 (2012) 335–350.

[44] L. Soucasse, Effets des transferts radiatifs sur les écoulements de convection naturelle dans une cavité différentiellement chauffée en régimes transitionnel et faiblement turbulent., Ph.D. thesis, École Centrale Paris, France (2013).
URL `https://tel.archives-ouvertes.fr/tel-00978507/document`

[45] S. Xin, P. Le Quéré, An extended Chebyshev pseudo-spectral benchmark for the 8:1 differentially heated cavity, Numerical Metholds in Fluids 40 (2002) 981–998.

[46] S. Xin, J. Chergui, P. Le Quéré, 3D spectral parallel multi-domain computing for natural convection flows, in: Springer (Ed.), Parallel Computational Fluid Dynamics, Lecture Notes in Computational Science and Engineering book series, Vol. 74, 2008, pp. 163–171.

[47] O. Shishkina, R. J. A. M. Stevens, S. Grossmann, D. Lohse, Boundary layer structure in turbulent thermal convection and its consequences for the required numerical resolution, New Journal of Physics 12 (2010) 075022.

[48] L. Soucasse, Ph. Rivière, A. Soufiani, Subgrid-scale model for radiative transfer in turbulent participating media, Journal of Computational Physics 257, Part A (2014) 442–459.

[49] E. Tric, G. Labrosse, M. Betrouni, A first incursion into the 3D structure of natural convection of air in a differentially heated cubic cavity, from

accurate numerical solutions, International Journal of Heat and Mass Transfer 43 (2000) 4043–4056.

[50] F. X. Trias, M. Soria, A. Oliva, C. D. Pérez-Segarra, Direct numerical simulation of a two- and three-dimensional turbulent natural convection flows in a differentially heated cavity of aspect ratio 4, Journal of Fluid Mechanics 586 (2007) 259–293.

[51] F. X. Trias, A. Gorobets, M. Soria, A. Oliva, Direct numerical simulation of a differentially heated cavity of aspect ratio 4 with Rayleigh numbers up to 10^{11}. Part I: Numerical methods and time-averaged flow, International Journal of Heat and Mass Transfer 53 (2010) 665–673.

[52] F. X. Trias, A. Gorobets, M. Soria, A. Oliva, Direct numerical simulation of a differentially heated cavity of aspect ratio 4 with Rayleigh numbers up to 10^{11}. Part II: Heat transfer and flow dynamics, International Journal of Heat and Mass Transfer 53 (2010) 674–683.

[53] M. Kaczorowski, K.-Q. Xia, Turbulent flow in the bulk of Rayleigh–Bénard convection: small-scale properties in a cubic cell, Journal of Fluid Mechanics 722 (2013) 596–617.

[54] A. Xu, L. Shi, H.-D. Xi, Lattice Boltzmann simulations of three-dimensional thermal convective flows at high Rayleigh number, International Journal of Heat and Mass Transfer 140 (2019) 359–370.

[55] A. Bejan, A. D. Kraus, Heat Transfer Handbook, H-John Wiley & Sons, 2003.

[56] I. Catton, The effect of insulating vertical walls on the onset of motion in a fluid heated from below, International Journal of Heat and Mass Transfer 15 (1972) 665.

[57] W. V. R. Malkus, The heat transport and spectrum of thermal turbulence, Proceedings of the Royal Society A 225 (1954) 196–212.

[58] J. J. Niemela, L. Skrbek, K. R. Sreenivasan, R. J. Donnelly, Turbulent convection at very high Rayleigh numbers, Nature 404 (2000) 837–840.

[59] A. Soufiani, Temperature turbulence spectrum for high-temperature radiating gases, Journal of Thermophysics 5 (4) (1991) 489–494.